

# Field effect transistor to enable registration of reaction energy pathways

Alexander E. Kuznetsov (✉ [kae@tcen.ru](mailto:kae@tcen.ru))

SMC "Technological Centre" <https://orcid.org/0000-0002-1333-5294>

Maria S. Andrianova

SMC "Technological Centre"

Evgeniy V. Kuznetsov

Institute of Nanotechnology of Microelectronics of the Russian Academy of Sciences

---

## Research Article

**Keywords:** Energy profile, energy pathway, field effect transistor, Gibbs free energy, reaction mechanisms, ISFET

**Posted Date:** October 27th, 2020

**DOI:** <https://doi.org/10.21203/rs.3.rs-95899/v1>

**License:**   This work is licensed under a Creative Commons Attribution 4.0 International License.

[Read Full License](#)

---

1 **Title: Field effect transistor to enable registration of reaction energy pathways**

2

3 Authors: Alexander E. Kuznetsov<sup>1\*</sup> (kae@tcen.ru), Mariia S. Andrianova<sup>1</sup>  
4 (smariika1987@gmail.com) and Evgeniy V. Kuznetsov<sup>2</sup> (ev\_kuznetsov@mail.ru).

5

6 Affiliations:

7 1. Scientific-Manufacturing Complex “Technological Centre”, 124498, Zelenograd, Moscow,  
8 Russia

9 2. Institute of Nanotechnology of Microelectronics of the Russian Academy of Sciences,  
10 115487, Moscow, Russia

11 \*Correspondence to: kae@tcen.ru (A.K.)

12

13 **Abstract:** Each chemical reaction has its own energy profile that represents the energy changes  
14 during the transformation of reactants into products. Together with other sources, it provides  
15 information about the reaction mechanism. Here, we show how a complementary metal-oxide-  
16 semiconductor (CMOS)–compatible field effect transistor can be used to register an energy  
17 pathway of a chemical reaction. As a proof of concept we record an energy profiles (energy  
18 changes vs. reaction coordinate) of 3,3',5,5'-tetramethylbenzidine oxidation catalyzed by  
19 horseradish peroxidase. This approach can be potentially extended to study other enzymatic and  
20 non-enzymatic reactions.

21 **Main Text:**

22 Understanding the mechanism of a chemical reaction makes it possible to control the  
23 course of the reaction, its direction, and its efficiency. Despite the clear significance of this  
24 knowledge, to date, energy profiles are assessed by indirect methods<sup>1-3</sup> combined with

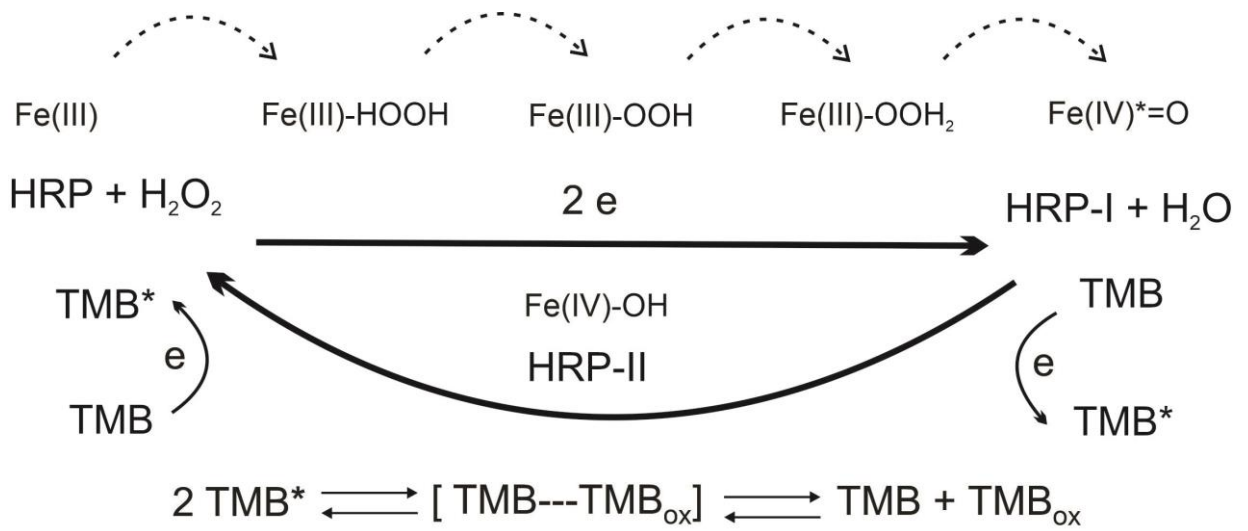
1 theoretical predictions by computer modeling methods <sup>4,5</sup>. A field effect transistor (FET) is a  
2 popular transducer for engineering sensors and biosensors. These sensors are capable of  
3 detecting small molecules <sup>6</sup>, various biomarkers <sup>7</sup>, molecule–molecule interactions <sup>8</sup>, and cell  
4 activity <sup>9</sup>. They were designed by replacing the metal gate of a metal-oxide-semiconductor FET  
5 (MOSFET) with an electrolyte solution and an immersed reference electrode. Historically, this  
6 design was called an ion-sensitive FET (ISFET) <sup>10</sup>. Most of the principles for detection by FET  
7 sensors proposed to date have been based on selective adsorption or increasing analyte  
8 concentration using ion-selective membranes at the electrolyte–field transistor interface, which  
9 lead to a change in the effective surface charge <sup>11</sup>. This charge changes the electrolyte–  
10 semiconductor potential, which is detected by the transistor. However, the electrolyte–  
11 semiconductor potential depends on the internal characteristics of the solution, which is the gate  
12 material. This fact is well known for MOSFETs, in which the threshold voltage of the transistor  
13 depends on the work function of the electrons from the gate material. Further, the work function  
14 of the material is determined by the chemical potential of the electrons. In the case of ISFETs,  
15 the gate is replaced by an electrolyte; as such, the threshold voltage depends on the chemical  
16 potential of the electrons in the solution,  $\mu_e$ .  $\mu_e$  is characterized by the equilibrium state of the  
17 redox reactions in solution (redox system) and corresponds to the oxidation–reduction potential  
18 on a vacuum scale:  $\mu_e = -neE_{redox}(vac. scale)$ , where  $E_{redox}(vac. scale)$  is the potential  
19 relative to the vacuum level, and  $n$  is the number of electrons involved in the redox reaction <sup>12</sup>.  
20 Therefore, changes in the component composition of the redox system, caused by the  
21 initialization of a homogeneous chemical reaction in solution, will be accompanied by a change  
22 in  $\mu_e$ . If the reaction rate is much lower than the rate of equilibrium established in the redox  
23 system, then the extent of the reaction  $\xi_r$  will be associated with the specific  $\mu_e$  value for each  
24 reaction. By initializing the reaction in the gate solution, we show that it is possible to measure  
25 the transient characteristics of  $\mu_e(t)$  in the system. Each extent of reaction  $\xi_r$  will correspond to  
26 the time  $t$  from the beginning of the reaction, such that transient “redox” reaction profiles can be

1 obtained. For the homogeneous redox reaction in which all solution components are involved,  
2 the relative changes in the chemical potential of the electrons are equal to the relative changes in  
3 Gibbs free energy during the reaction (refer to supplementary materials).

4 To support our hypothesis we investigate energy changes in gate solution during  
5 horseradish peroxidase (HRP) catalytic cycle. It is well known that enzymatic reactions have  
6 complicated energy profiles that are interest of science and could be a good demonstration as a  
7 proof of concept.

8 In this study we used a fully depleted silicon-on-insulator (FD-SOI),  $100 \times 100 \mu\text{m}$ , n-  
9 channel ISFET with a  $\text{SiO}_2$ -sensitive area and a platinum electrode (Fig.S1). The sensors were  
10 designed for operation in subthreshold transistor mode and were fabricated according to the 1.2  
11  $\mu\text{m}$  complementary metal-oxide-semiconductor (CMOS) standard process, with a sensitivity of  
12 40 mV/pH and an average subthreshold swing value of  $137.3 \pm 12.1 \text{ mV/dec}$  (Fig. S2). The  
13 reaction considered was that of 3,3',5,5'-tetramethylbenzidine (TMB) oxidation catalyzed by  
14 horseradish peroxidase (HRP). HRP is a hemoprotein peroxidase that catalyzes the oxidation of a  
15 broad range of substrates and is extensively used in the fields of immunochemistry, biocatalysis,  
16 bioremediation, and medicine<sup>13,14</sup>. The general scheme of the HRP catalytic cycle with  $\text{H}_2\text{O}_2$   
17 and TMB is presented in Fig. 1.

1



2

3 Fig. 1 Reaction scheme for the HRP reaction with TMB <sup>15,16</sup>.

4

5 The catalytic cycle includes the donation of two electrons to hydrogen peroxide by  
 6 hemoprotein, forming Compound I (HRP-I)—a first two-electron transfer reaction. Next, HRP-I  
 7 accepts one electron from the second substrate (TMB), forming Compound II (HRP-II). HRP-II  
 8 recovers to the native state by taking an additional electron from a second TMB molecule <sup>15</sup>.

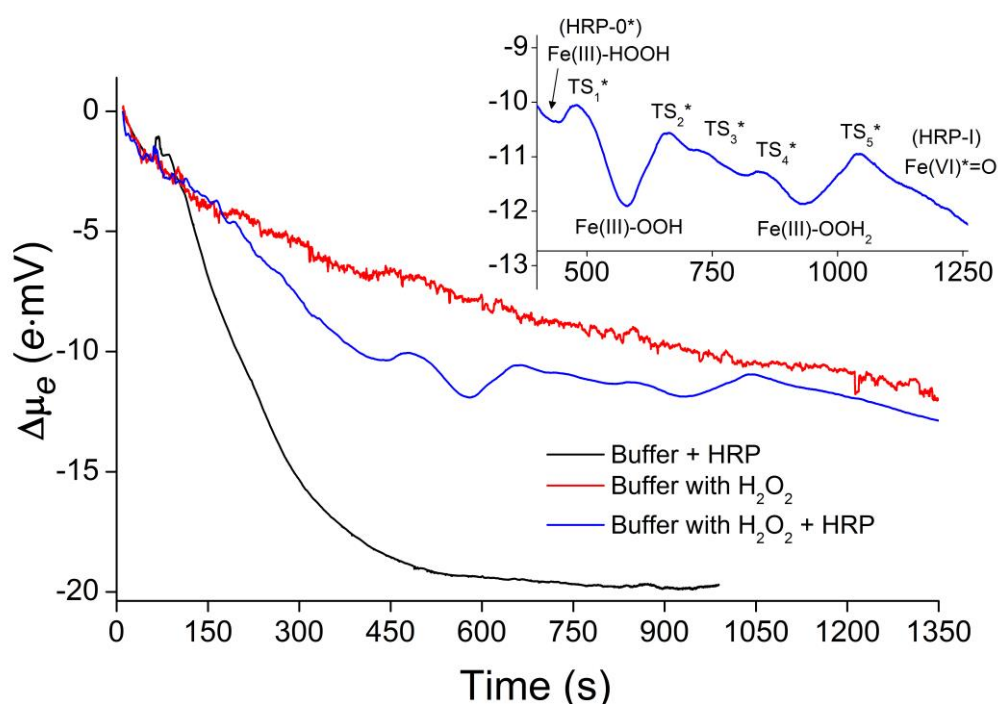
9 The formation of HRP-I does not require a second substrate <sup>17</sup>, and this makes it possible  
 10 to separate the investigation of enzyme oxidation and reduction. To study this part of the HRP  
 11 cycle, we initiated an HRP oxidation reaction by simply adding HRP and H<sub>2</sub>O<sub>2</sub> to a citrate–  
 12 phosphate buffer in a well-like structure formed on a chip. The time-dependent changes in  $\mu_e$  in  
 13 the well after reaction initiation was monitored by measuring relative changes in the ISFET  $I_{DS}$   
 14 over time.

15 The result of these experiments is shown in Fig. 2. In the case of H<sub>2</sub>O<sub>2</sub>–buffer mixture, a  
 16 straight line with a low drift of ~0.4 mV/min was observed. For HRP injection, a typical  
 17 potential drop curve with base stabilization was observed. The value of the final potential drop  
 18 was correlated with the added enzyme concentration and decreased with the reduction in enzyme

1 concentration. The addition of 1 pM of HRP to 520  $\mu\text{M}$   $\text{H}_2\text{O}_2$  had no influence on the potential  
2 behavior (data not shown). We gradually increased the enzyme concentration to increase the  
3 number of enzyme redox states in solution. When the HRP concentration exceeded 3.8  $\mu\text{M}$ , the  
4 redox equilibrium shift in the gate solution become detectable by the ISFET. The observed time-  
5 dependent change in  $\mu_e$  was reproducible and exhibited specific pattern, showing a sequence of  
6 different energy states during the reaction.

7 Today, it is largely accepted that the reaction of HRP with  $\text{H}_2\text{O}_2$  proceeds via a Poulos–  
8 Kraut-based mechanism<sup>18</sup> and has three intermediate states. At the very early stages of the  
9 catalytic process, the protonated  $\text{H}_2\text{O}_2$  molecule coordinates to the heme iron with formation of  
10 intermediate  $[\text{Fe}(\text{III})\text{--HOOH}]$  (HRP-0\*). It is believed that this intermediate is required to make  
11 the hydrogen peroxide sufficiently acidic to be deprotonated by the distal His42 residue<sup>19</sup>,  
12 forming the next intermediate state  $[\text{Fe}(\text{III})\text{--OOH}]$ , called Compound 0 (HRP-0)<sup>20</sup>. The released  
13 proton is then delivered by His42 to the terminal oxygen of the ferric hydroperoxide, forming  
14 complex  $[\text{Fe}(\text{III})\text{--OOH}_2]$ , containing a water-leaving group.  $\text{H}_2\text{O}$  debonding leads to cleavage of  
15 the O–O bond, and the  $[\text{Fe}(\text{III})\text{--OOH}_2]$  intermediate is transformed to  $[\text{Fe}(\text{IV})\text{=O}]^*$ , that is,  
16 HRP-I<sup>21</sup>.

17 Thus the obtained results are consistent with the Poulos–Kraut mechanism for HRP-I  
18 formation. The obtained energy pathway has three minima, corresponding to three intermediate  
19 iron states in the catalytic core. The characteristic time between registration of the first minimum  
20 (corresponding to HRP-0\*) and end of the reaction (HRP-I formation) was  $\sim 750$  s. Similar times  
21 for the reaction of  $\text{H}_2\text{O}_2$  with HRP were reported previously using the stopped-flow technique<sup>21</sup>.



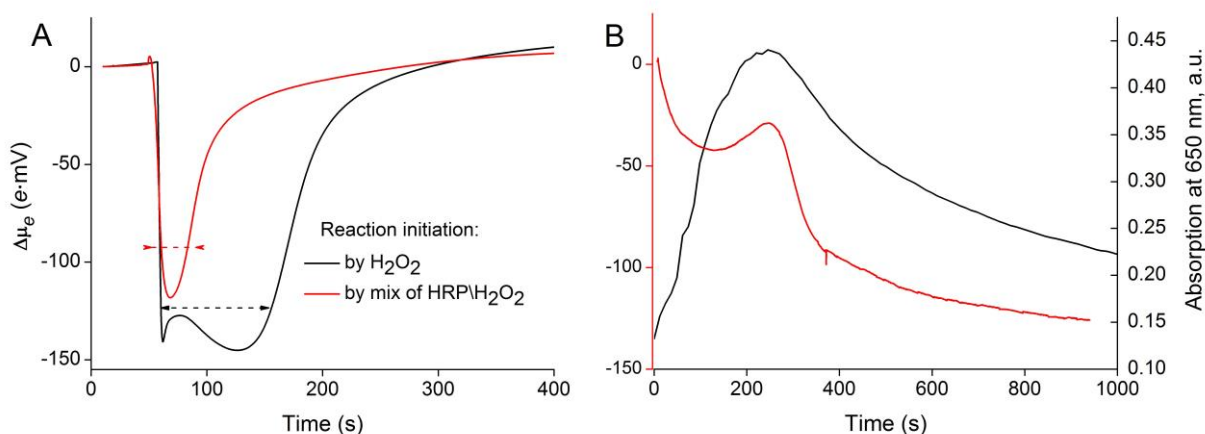
1

2 Fig. 2 Relative change in chemical potential of electrons,  $\mu_e$ , in gate solution during initiation of  
 3 the reaction between HRP and  $\text{H}_2\text{O}_2$ . Black: response to addition of HRP to 100 mM citrate–  
 4 phosphate buffer (pH 5.5) at 60 s to achieve a final concentration of 3.8  $\mu\text{M}$ ; red: 100 mM  
 5 citrate–phosphate (pH 5.5) buffer containing 520  $\mu\text{M}$   $\text{H}_2\text{O}_2$  without HRP; blue: response to  
 6 addition of HRP to 100 mM citrate–phosphate buffer (pH 5.5) containing 520  $\mu\text{M}$   $\text{H}_2\text{O}_2$  at 60 s  
 7 to achieve a final concentration of 3.8  $\mu\text{M}$ . Inset: enlarged part of region corresponding to the  
 8 energy pathway of HRP-I formation.

9

10 Currently, the rate-limiting step in HRP-I formation is still being studied. The energy  
 11 profile data obtained demonstrates that after  $\text{H}_2\text{O}_2$  coordination in the catalytic core, the process  
 12 of deprotonation with formation of  $[\text{Fe}(\text{III})\text{-OOH}]$  and the O–O bond cleavage of  $[\text{Fe}(\text{III})\text{-}$   
 13  $\text{OOH}_2]$  are faster than the conversion from intermediate  $[\text{Fe}(\text{III})\text{-OOH}]$  to  $[\text{Fe}(\text{III})\text{-OOH}_2]$ .  
 14 Moreover, the ISFET is capable of detecting additional transition states extended in time  
 15 corresponding to the proton flow in His170–heme–OOH–His42–Arg38 in the binding pocket<sup>22</sup>.

1           Figure 3A demonstrates the difference in energy profiles for TMB oxidation by HRP and  
 2 by HRP-I. As HRP and H<sub>2</sub>O<sub>2</sub> react in the absence of the second substrate, their preincubation  
 3 accelerates the oxidation of the second substrate owing to the HRP-I accumulation. Moreover,  
 4 with the preliminary incubation, the obtained profiles lack the stage of HRP-I formation that is  
 5 present for the full reaction in the potential well. It was observed that preincubation of HRP with  
 6 H<sub>2</sub>O<sub>2</sub> for less than 1 min leads to a decrease in the time before system energy begins to grow.



7

8 Fig. 3 (A) Effect of preincubation of HRP with H<sub>2</sub>O<sub>2</sub> on the obtained signal. Reaction conditions:  
 9 5  $\mu$ M TMB, 520  $\mu$ M H<sub>2</sub>O<sub>2</sub>, 3.8  $\mu$ M HRP in 100 mM pH 5.5 citrate–phosphate buffer solution.  
 10 (B) Red: real-time FET-sensor response for the reaction of 1.8 nM HRP with 200  $\mu$ M H<sub>2</sub>O<sub>2</sub> and  
 11 500  $\mu$ M TMB; black: formation and decay of charge-transfer complex in microplate reader at the  
 12 same conditions.

13

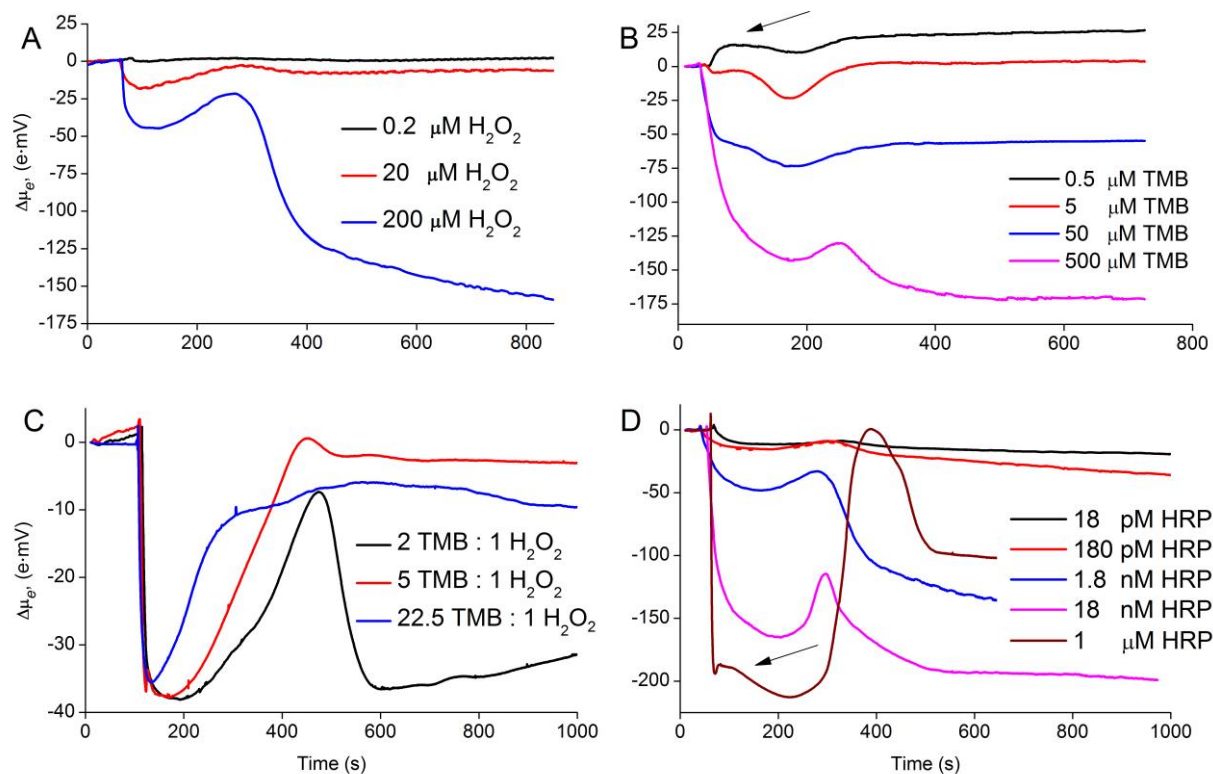
14           The detected energy growth corresponds to TMB\* and HRP-II formation in the gate  
 15 solution; this assumption was confirmed by spectrophotometric studies. According to the TMB  
 16 oxidation mechanism, free radical forms of TMB\* and HRP-II are formed after interaction with  
 17 HRP-I. TMB\* exists in an equilibrium with the intermediate charge-transfer complex (the  
 18 complex of the diamine (electron donor, TMB) and the diimine (electron acceptor, TMB-  
 19 oxidized)) (Fig. 1), which can be detected by monitoring the adsorption at 650 nm<sup>16</sup>. The

1 formation and decay of cation radicals follow a time course similar to that for the charge-transfer  
2 complex. The energy peak detected by ISFET coincides with times for existence of the charge-  
3 transfer complex as detected by adsorption measurements at similar reaction conditions (Fig.  
4 3B).

5 Variation in substrate concentrations leads to predictable peak changes corresponding to  
6 the established mechanism for TMB oxidation by HRP. At the start of peak formation, the height  
7 and peak area grew with an increase in the substrate concentrations (Fig. 4). After addition of  
8 H<sub>2</sub>O<sub>2</sub> to the well containing 7.4 nM HRP and 500 μM TMB to achieve a final concentration of  
9 0.2 μM, there was no noticeable change in  $\Delta\mu_e$ . An increase in H<sub>2</sub>O<sub>2</sub> to 20 μM led to a typical  
10 peak that became larger after addition of 200 μM H<sub>2</sub>O<sub>2</sub> to the same concentrations of HRP and  
11 TMB (Fig. 4A). It is notable that at low H<sub>2</sub>O<sub>2</sub> concentrations in the presence of 500 μM TMB  
12 and 7.4 nM HRP, we did not observe the stage of HRP-I formation.

13

1



2

3 Fig. 4 Real-time FET-sensor response for TMB oxidation by HRP at different reagent  
4 concentrations under reaction initiation by addition of H<sub>2</sub>O<sub>2</sub>. (A) Various H<sub>2</sub>O<sub>2</sub> concentrations at  
5 7.4 nM HRP, 500 μM TMB, reaction initiation at 60 s. (B) Various TMB concentrations at 18  
6 nM HRP, 200 μM H<sub>2</sub>O<sub>2</sub>, reaction initiation at 35 s; arrow shows the area of HRP-I formation  
7 reaction. (C) Various TMB concentrations at 5 nM HRP, 200 μM H<sub>2</sub>O<sub>2</sub>, reaction initiation at 113  
8 s. (D) Various HRP concentrations at 500 μM TMB, 200 μM H<sub>2</sub>O<sub>2</sub>, reaction initiation at 50 s;  
9 arrow shows the area of HRP-I formation reaction.

10

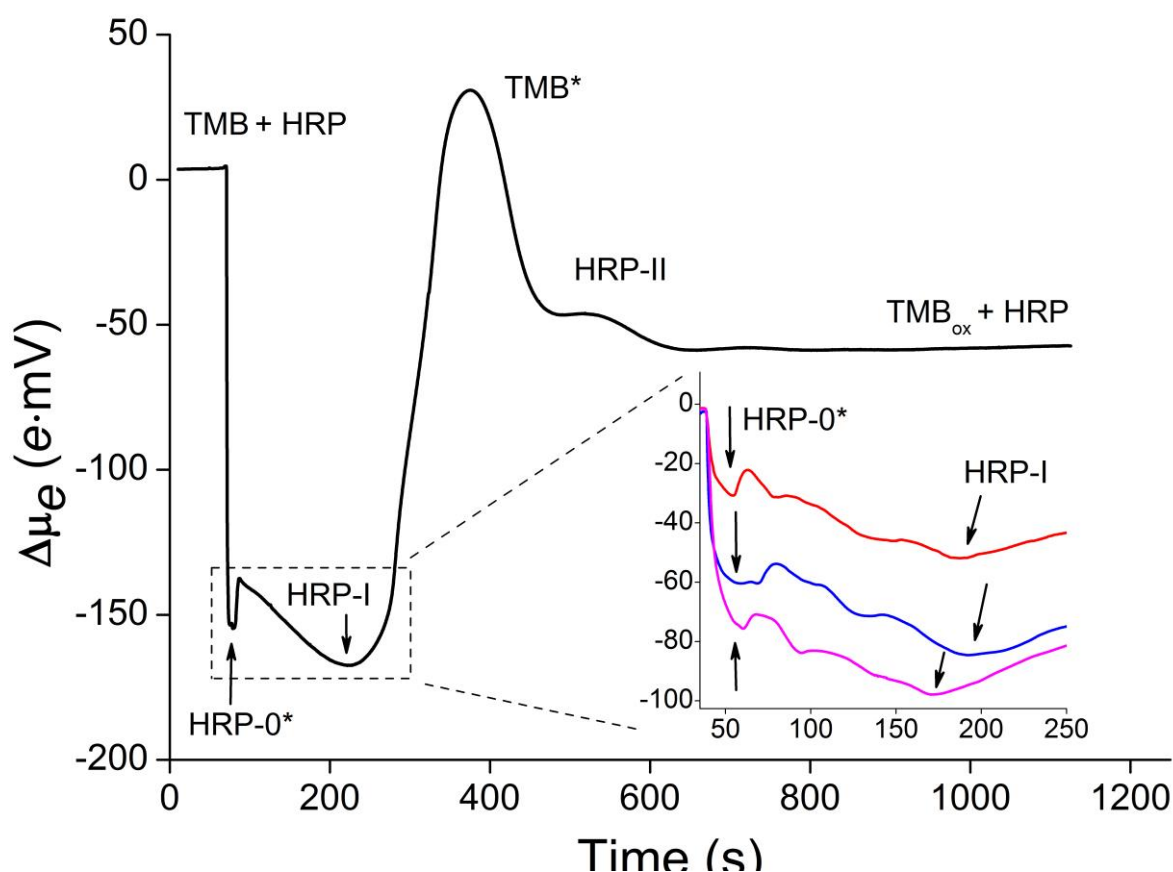
11 However, at low TMB concentrations under relatively high H<sub>2</sub>O<sub>2</sub> concentrations, the  
12 peak corresponding to HRP-I formation was noticeable. With an increase in TMB concentration  
13 in solution, the HRP-I formation signal became less detectable, whereas the peak corresponding  
14 to TMB oxidation grew (Fig. 4B).

1           According to the reaction mechanism (Fig. 1), the oxidation of one molecule of TMB  
2   requires half a molecule of  $\text{H}_2\text{O}_2$ <sup>23</sup>. At a 2:1 ratio of TMB: $\text{H}_2\text{O}_2$ , corresponding to maximum  
3   charge-transfer complex formation conditions<sup>16</sup>, we observed the largest peak formation and its  
4   full decay; additionally, the final color in the well became yellow, indicating that the reaction  
5   finished with the formation of TMB-oxidized diamine when signal recording was stopped. With  
6   increasing TMB concentration, we observed that after reaching the peak top point, the potential  
7   stopped falling, and at a higher ratio (TMB: $\text{H}_2\text{O}_2$  ratio of 22.5:1) it plateaued at the top point,  
8   indicating that not all TMB oxidized to the final diamine form (Fig. 4C). At these conditions, the  
9   solution in the well changed from blue to green, indicating that the charge-transfer complex still  
10   existed in the final product mixture. Interestingly, the potential minimum corresponding to HRP-  
11   I formation decreased in time with an increase in the ratio (Fig. 4C). These results demonstrate  
12   that energy changes in the gate after HRP-I formation are governed by TMB\* radical  
13   accumulation and disproportionation with formation of the final diamine form.

14           To increase the contribution of HRP intermediate states in the general energy  
15   rearrangement, we varied the enzyme concentration under fixed substrate concentrations. Figure  
16   4D demonstrates that the slopes of the curves increase with increasing HRP concentration. The  
17   peak height increased from 10 mV to 200 mV when the final enzyme concentration changed  
18   from 18 pM to 1  $\mu\text{M}$ . Thus, an increase in enzyme leads to faster TMB\* accumulation and decay  
19   in the system. Another noticeable effect is the appearance of HRP intermediate states in the  
20   redox profile at high enzyme concentrations against the background of TMB\* evolution in the  
21   system. The small peak corresponding to HRP-I formation was reproducible at the large enzyme  
22   concentrations (1–10  $\mu\text{M}$ ) in the gate solution at 500  $\mu\text{M}$  TMB, 200  $\mu\text{M}$   $\text{H}_2\text{O}_2$ . However, the  
23   reaction rates did not permit high resolution of the intermediate and transition states in this area  
24   to be achieved. High resolution in this area (energy change vs. time) throughout the reaction was  
25   achieved by lowering TMB concentrations in the gate solution (Fig. 5) under relatively high  
26   enzyme concentrations. At these conditions, the pattern corresponding to HRP-I formation

1 before TMB oxidation was similar to the pattern obtained for the half-reaction of HRP with  $H_2O_2$   
2 (Fig. 3). The pattern obtained at lower TMB concentrations have the same three minima, but  
3 signal oscillations were substantially compressed in time compared with the half-reaction curves.  
4 Thus, Fig. 5 shows the final energy trajectory of enzymatic reaction in the gate solution. This  
5 trajectory includes intermediate steps during HRP-I formation under interactions with  $H_2O_2$  as  
6 well as the accumulation of radical TMB\* during HRP-II formation. The high impact of TMB\*  
7 did not permit the detection of intermediate states in the catalytic core during  $[Fe(IV)=O]^*$   
8 transformation to  $[Fe(IV)-OH]$ . However, with TMB\* decay in the system, we observed an  
9 additional shell in the profile that may correspond to residual concentration of HRP-II and its  
10 transformation to native HRP. The stabilization of the curve after 700 s indicates that the  
11 chemical reactions in the gate finished and the enzyme returned to its native form.

12



1

2 Fig 5 Energy pathway equal to the relative changes in Gibbs free energy during the reaction of  
 3 TMB oxidation catalyzed by HRP with suggested intermediates (50  $\mu\text{M}$  HRP, 500  $\mu\text{M}$  TMB,  
 4 200  $\mu\text{M}$   $\text{H}_2\text{O}_2$ ). Reaction was initiated by addition of  $\text{H}_2\text{O}_2$  at 70 s. Enlarged area: 0.05  $\mu\text{M}$  HRP,  
 5 200  $\mu\text{M}$   $\text{H}_2\text{O}_2$ ; red, 70  $\mu\text{M}$  TMB; blue, 90  $\mu\text{M}$  TMB; purple, 200  $\mu\text{M}$  TMB.

6

## 7 Conclusion

8 In this work, we introduce a novel and promising experimental method for recording  
 9 energy changes during chemical reactions. As a proof of concept to support our hypothesis we  
 10 record energy profiles of HRP catalytic reactions under different conditions. Our findings  
 11 demonstrate the possibility of using ISFET sensors to study the energy pathway during reactions.  
 12 In the case of redox reactions occurring in the gate, these changes under constant pressure and  
 13 temperature are equal to the changes in the Gibbs free energy of the system caused by the  
 14 chemical reaction. The proposed method allows the detection of transition and intermediate steps

1 during the reaction and can be used to study the influence of different conditions on the reaction  
2 mechanism.

3

4 Taken together, these opportunities can provide new insights into the nature of chemical  
5 reactions.

6

## 7 **Methods**

### 8 FET Sensor Setup

9 Fully depleted silicon-on-insulator (FD SOI) ISFETs with a SiO<sub>2</sub>-sensitive area were  
10 fabricated according to the 1.2 μm CMOS standard process, in which a Pt electrode was used as  
11 the redox electrode. All experiments were performed in well structures formed on a chip surface.  
12 Between measurements, the well containing the sensors was carefully washed, and the surface of  
13 the Pt electrode was cleaned in a Caro's acid solution. The system was stabilized by immersing  
14 the sensors in buffer solution and holding the structure at a constant voltage bias in subthreshold  
15 mode for 900 s.

16

### 17 Electrical Measurements

18 Measurements of  $\Delta\mu_e$  during the chemical reaction were carried out using the ISFET in  
19 subthreshold mode.

20 The electrical potential at the ISFET surface (i.e., the solution–oxide interface) corresponds  
21 to the metal gate potential in a conventional MOSFET. Therefore, the ISFET subthreshold  
22 current  $I_{DS}$  depends on the surface potential  $\varphi_S$ , as in the MOSFET, at source voltage  $V_{SB} = 0$   
23 and drain-source voltage  $V_{DS} > 4\varphi_t$  as follows<sup>24</sup>:

$$24 \quad I_{DS} = I_0 \frac{W}{L} n \cdot \exp \frac{(\varphi_S - V_t)}{n_0 \varphi_t} \quad (1)$$

1 where  $W/L$  is the transistor channel ratio,  $V_t$  the threshold voltage,  $n_0$  the slope factor,  $I_0$  the  
2 current constant, and  $\varphi_t$  the thermal voltage.

3 Therefore, for small changes in  $\Delta I_{DS}$ , it follows from (1) that

$$4 \quad \Delta I_{DS}(\Delta\varphi_S) \approx \frac{dI_{DS}}{d\varphi_S} \Delta\varphi_S = I_{DS} \frac{\Delta\varphi_S}{n_0\varphi_t} \quad (2)$$

5 The  $\varphi_S$  value in an ISFET can be controlled through the voltage on the electrode,  $U$ , which can  
6 be written in the form of (S.13) as

$$7 \quad \Delta I_{DS}(\Delta U) \approx I_{DS} \frac{\Delta U}{n_0\varphi_t} \frac{d\varphi_S}{dU} \quad (3)$$

8 Then, from experimental measurements and using (3), it is possible to determine the ISFET  
9 slope factor  $n = n_0 \left(\frac{d\varphi_S}{dU}\right)^{-1}$ . As shown in the Supplementary Information, changes in  $\Delta\mu_e$  with  
10 fixed  $U$  are equivalent to changes in  $U$  with fixed  $\mu_e$ . Thus, for a fixed  $U$ , a small change in  $\Delta\mu_e$   
11 (S.14) can be expressed as

$$12 \quad \frac{\Delta\mu_e}{e} \approx \frac{\Delta I_{DS}}{I_{DS}} n\varphi_t \quad (4)$$

13 When the reaction was initialized, a small change in  $\Delta\mu_e$  was ensured by implementing a  
14 relatively small discrete time between measurements (in the given measurements,  $\Delta t = 100$  ms  
15 would be sufficient):

$$16 \quad \frac{\Delta\mu_e^{(j)}(\Delta t)}{e} = \frac{\Delta I_{DS}^{(j)}}{I_{DS}^{(j)}} n\varphi_t \quad (5)$$

17 where  $\Delta\mu_e^{(j)}$  and  $\Delta I_{DS}^{(j)}$  are the changes in values at the  $j$ th step of the measurement time.

18 Measurements were made on an Agilent B1500A semiconductor device analyzer and a  
19 Cascade PM5 probe station using Agilent VEE Pro software.

## 1 **Funding:**

2 This work was supported by the Russian Science Foundation (project #17-79-20383).

## 3 **Data availability**

4 The data that support the findings of this study are available from the corresponding author upon  
5 reasonable request.

## 6 **References**

- 7 1. Ha, T. *et al.* Probing the interaction between two single molecules: fluorescence  
8 resonance energy transfer between a single donor and a single acceptor. *Proc. Natl. Acad. Sci.*  
9 **93**, 6264–6268 (1996).
- 10 2. P Palmer, A. G. NMR Characterization of the Dynamics of Biomacromolecules. *Chem.*  
11 *Rev.* **104**, 3623–3640 (2004).
- 12 3. J Jensen, M. R., Zweckstetter, M., Huang, J. & Blackledge, M. Exploring Free-Energy  
13 Landscapes of Intrinsically Disordered Proteins at Atomic Resolution Using NMR Spectroscopy.  
14 *Chem. Rev.* **114**, 6632–6660 (2014).
- 15 4. Kosloff, R. Time-dependent quantum-mechanical methods for molecular dynamics. *J.*  
16 *Phys. Chem.* **92**, 2087–2100 (1988).
- 17 5. Field, M. J., Bash, P. A. & Karplus, M. A combined quantum mechanical and molecular  
18 mechanical potential for molecular dynamics simulations. *J. Comput. Chem.* **11**, 700–733  
19 (1990).
- 20 6. Nakatsuka, N. *et al.* Aptamer-field-effect transistors overcome Debye length limitations  
21 for small-molecule sensing. *Science* **362**, 319–324 (2018).
- 22 7. Stern, E. *et al.* Label-free biomarker detection from whole blood. *Nat. Nanotechnol.* **5**,  
23 138–42 (2010).
- 24 8. Wang, W. U., Chen, C., Lin, K., Fang, Y. & Lieber, C. M. Label-free detection of small-  
25 molecule-protein interactions by using nanowire nanosensors. *Proc. Natl. Acad. Sci. U. S. A.*  
26 **102**, 3208–12 (2005).
- 27 9. Chen, K.-I., Li, B.-R. & Chen, Y.-T. Silicon nanowire field-effect transistor-based  
28 biosensors for biomedical diagnosis and cellular recording investigation. *Nano Today* **6**, 131–154  
29 (2011).
- 30 10. Bergveld, P. Development of an Ion-Sensitive Solid-State Device for Neurophysiological  
31 Measurements. *IEEE Trans. Biomed. Eng.* **BME-17**, 70–71 (1970).
- 32 11. Kaisti, M. Detection principles of biological and chemical FET sensors. *Biosens.*  
33 *Bioelectron.* **98**, 437–448 (2017).

- 1 12. Khan, S. U. M., Kainthla, R. C. & Bockris, J. O. M. The redox potential and the Fermi  
2 level in solution. *J. Phys. Chem.* **91**, 5974–5977 (1987).
- 3 13. Krainer, F. W. & Glieder, A. An updated view on horseradish peroxidases: recombinant  
4 production and biotechnological applications. *Appl. Microbiol. Biotechnol.* **99**, 1611–1625  
5 (2015).
- 6 14. Veitch, N. C. Horseradish peroxidase: a modern view of a classic enzyme.  
7 *Phytochemistry* **65**, 249–259 (2004).
- 8 15. Urlacher, V. Peroxidases and Catalases: Biochemistry, Biophysics, Biotechnology and  
9 Physiology. By H. Brian Dunford. *ChemBioChem* **11**, 1782–1783 (2010).
- 10 16. Josephy, P. D., Eling, T. & Mason, R. P. The horseradish peroxidase-catalyzed oxidation  
11 of 3,5,3',5'-tetramethylbenzidine. Free radical and charge-transfer complex intermediates. *J.*  
12 *Biol. Chem.* **257**, 3669–75 (1982).
- 13 17. Roberts, J. E., Hoffman, B. M., Rutter, R. & Hager, L. P. Electron-nuclear double  
14 resonance of horseradish peroxidase compound I. Detection of the porphyrin pi-cation radical. *J.*  
15 *Biol. Chem.* **256**, 2118–21 (1981).
- 16 18. Poulos, T. L. & Kraut, J. The stereochemistry of peroxidase catalysis. *J. Biol. Chem.* **255**,  
17 8199–205 (1980).
- 18 19. Tanaka, M., Ishimori, K., Mukai, M., Kitagawa, T. & Morishima, I. Catalytic Activities  
19 and Structural Properties of Horseradish Peroxidase Distal His42 → Glu or Gln Mutant †.  
20 *Biochemistry* **36**, 9889–9898 (1997).
- 21 20. Baek, H. K. & Van Wart, H. E. Elementary steps in the formation of horseradish  
22 peroxidase compound I: direct observation of compound 0, a new intermediate with a  
23 hyperporphyrin spectrum. *Biochemistry* **28**, 5714–5719 (1989).
- 24 21. Rodríguez-López, J. N. *et al.* Mechanism of reaction of hydrogen peroxide with  
25 horseradish peroxidase: identification of intermediates in the catalytic cycle. *J. Am. Chem. Soc.*  
26 **123**, 11838–47 (2001).
- 27 22. Derat, E. & Shaik, S. The Poulos–Kraut Mechanism of Compound I Formation in  
28 Horseradish Peroxidase: A QM/MM Study. *J. Phys. Chem. B* **110**, 10526–10533 (2006).
- 29 23. Marquez, L. A. & Dunford, H. B. Mechanism of the Oxidation of 3,5,3',5'-  
30 Tetramethylbenzidine by Myeloperoxidase Determined by Transient- and Steady-State Kinetics  
31 †. *Biochemistry* **36**, 9349–9355 (1997).
- 32 24. Schneider, M. C. & Galup-Montoro, C. *CMOS Analog Design Using All-Region*  
33 *MOSFET Modeling*. (Cambridge University Press, 2010). doi:10.1017/CBO9780511803840

# Figures

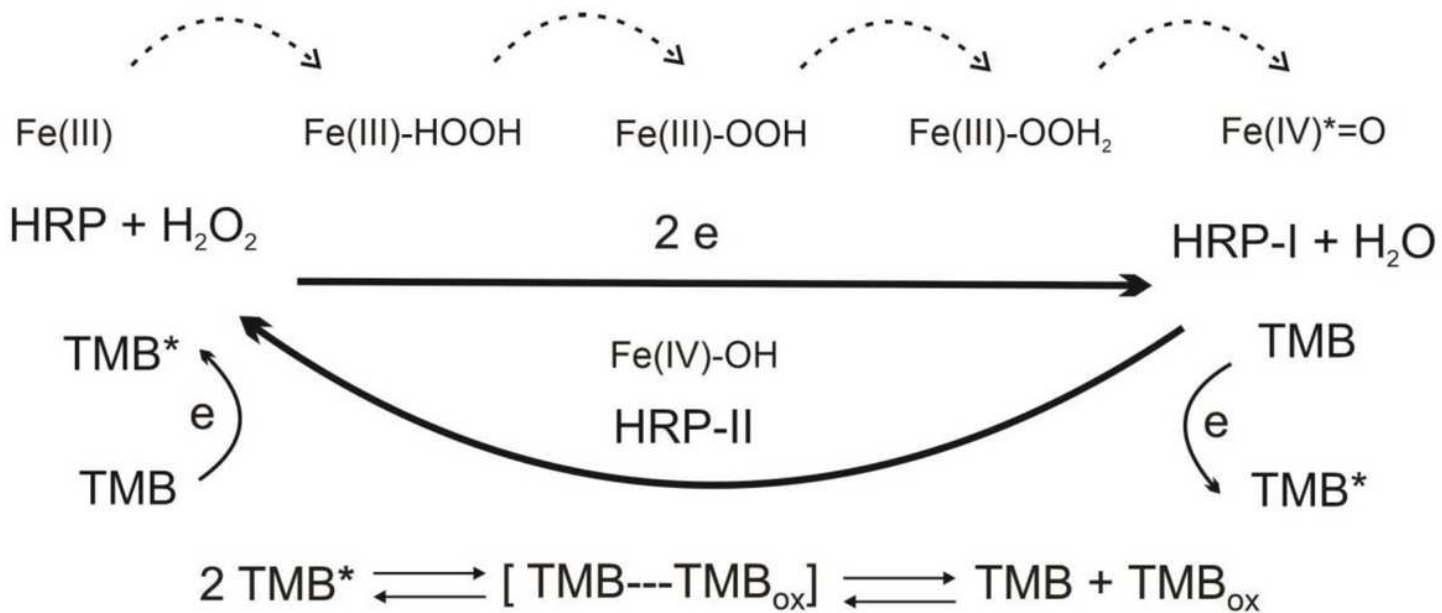
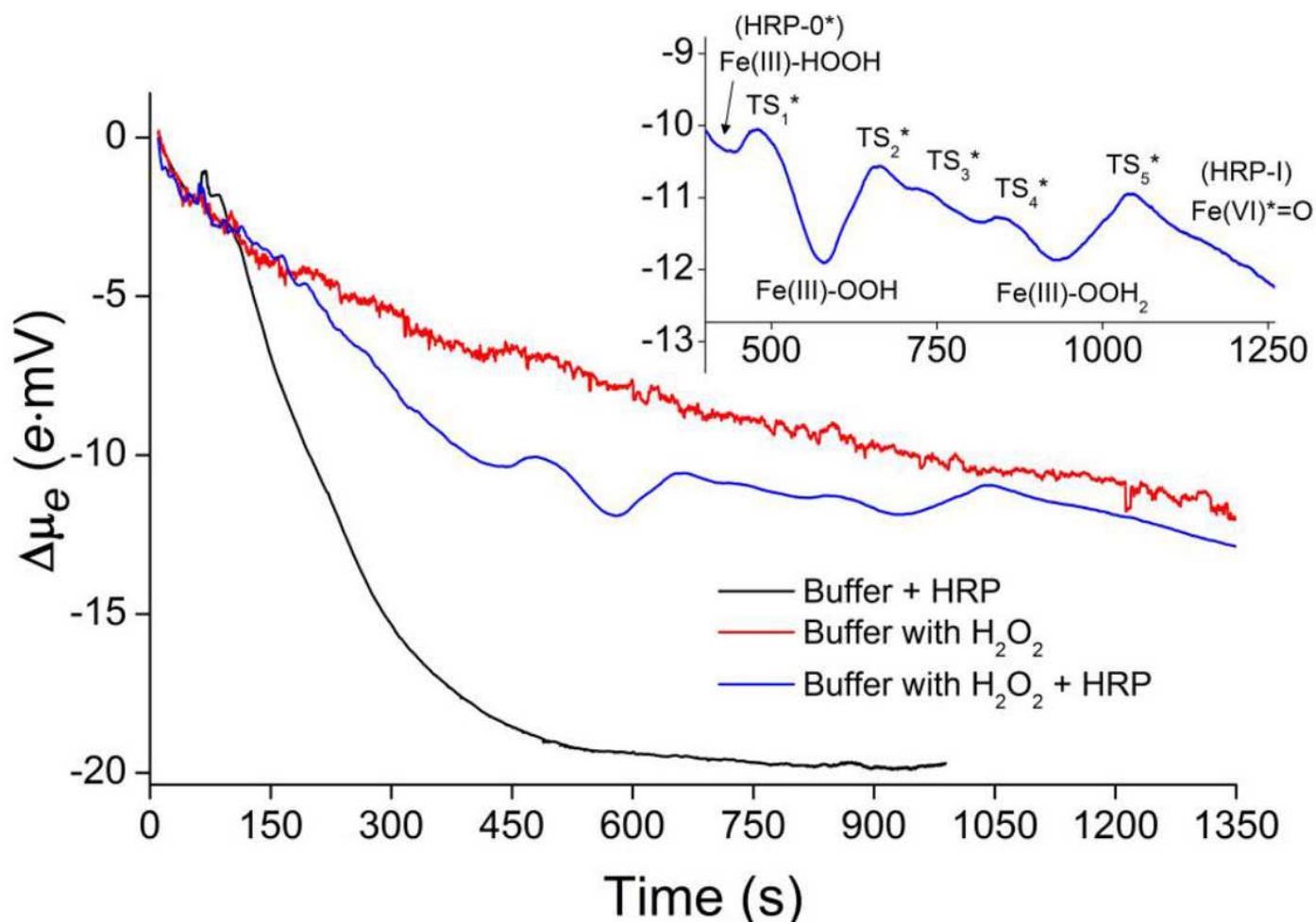


Figure 1

Reaction scheme for the HRP reaction with TMB 15,16.



**Figure 2**

Relative change in chemical potential of electrons,  $\Delta\mu_e$ , in gate solution during initiation of the reaction between HRP and H<sub>2</sub>O<sub>2</sub>. Black: response to addition of HRP to 100 mM citrate–phosphate buffer (pH 5.5) at 60 s to achieve a final concentration of 3.8  $\mu$ M; red: 100 mM citrate–phosphate (pH 5.5) buffer containing 520  $\mu$ M H<sub>2</sub>O<sub>2</sub> without HRP; blue: response to addition of HRP to 100 mM citrate–phosphate buffer (pH 5.5) containing 520  $\mu$ M H<sub>2</sub>O<sub>2</sub> at 60 s to achieve a final concentration of 3.8  $\mu$ M. Inset: enlarged part of region corresponding to the energy pathway of HRP-I formation.

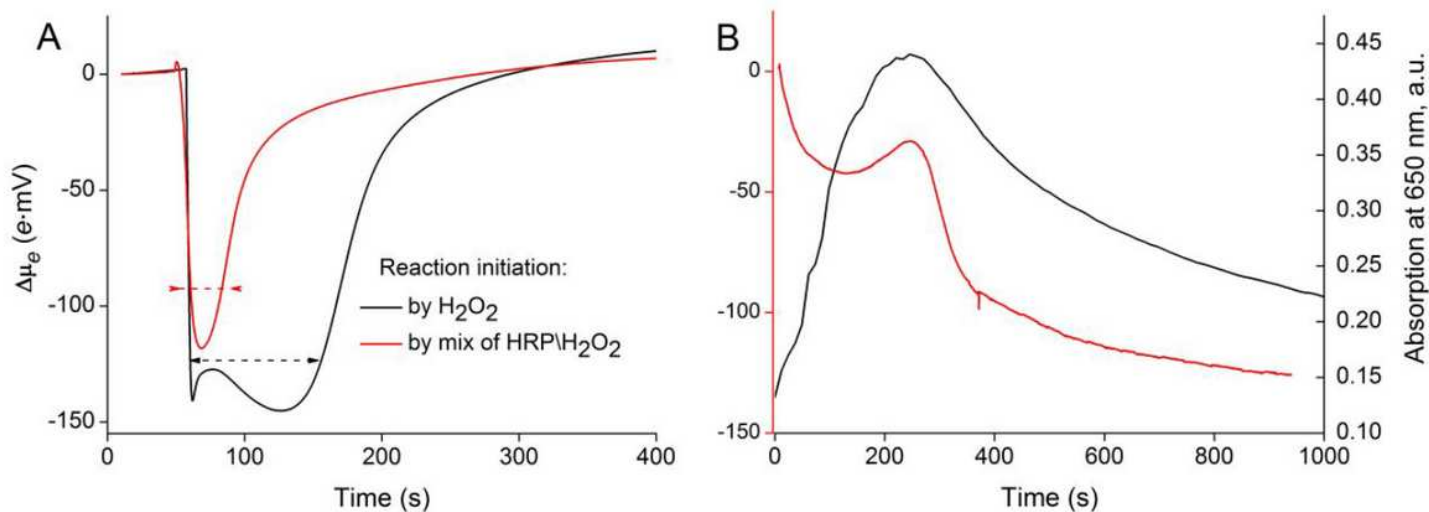


**Figure 3**

(A) Effect of preincubation of HRP with  $H_2O_2$  on the obtained signal. Reaction conditions: 5  $\mu M$  TMB, 520  $\mu M$   $H_2O_2$ , 3.8  $\mu M$  HRP in 100 mM pH 5.5 citrate-phosphate buffer solution. (B) Red: real-time FET-sensor response for the reaction of 1.8 nM HRP with 200  $\mu M$   $H_2O_2$  and 500  $\mu M$  TMB; black: formation and decay of charge-transfer complex in microplate reader at the same conditions.

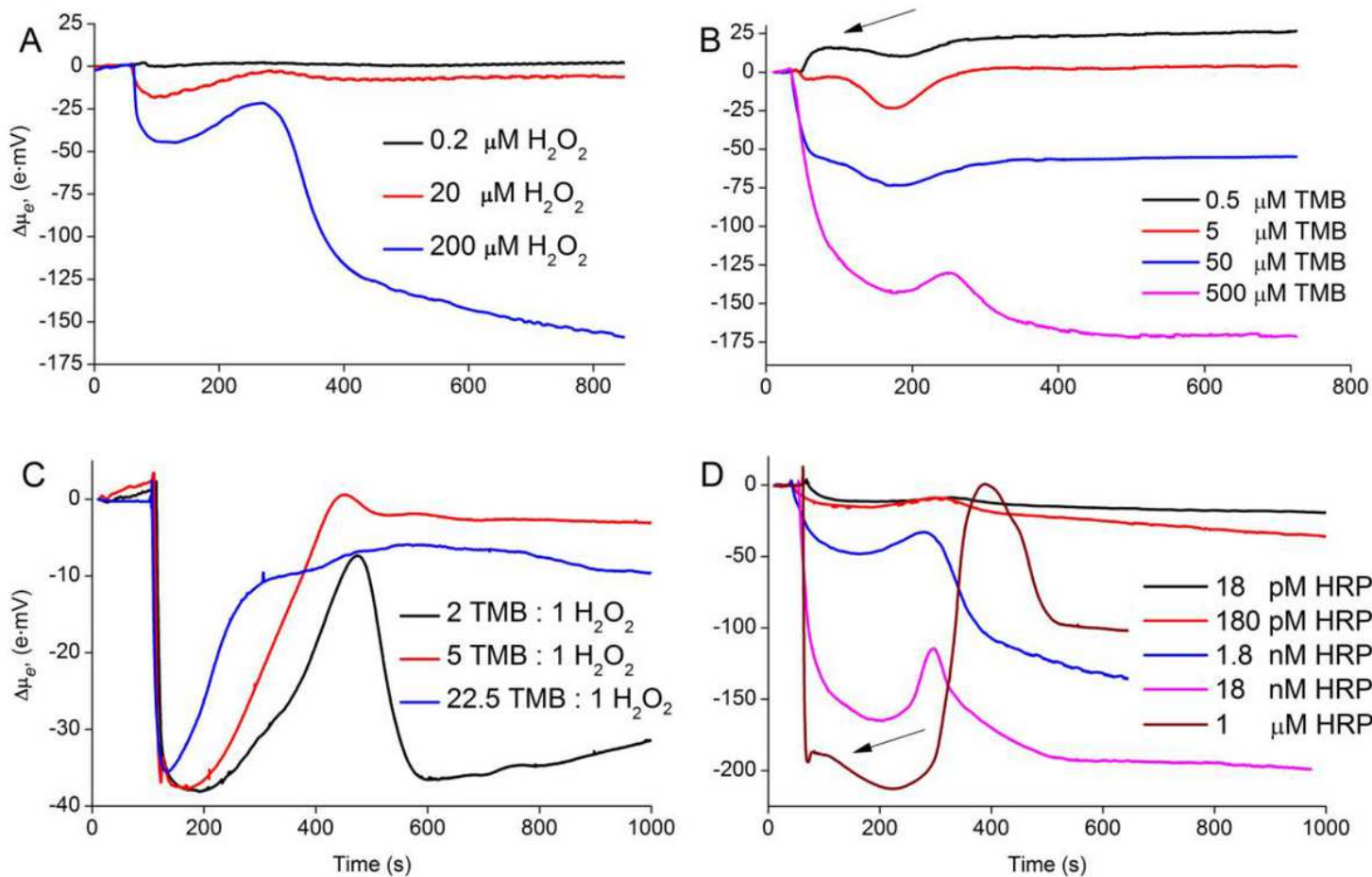


**Figure 4**

Real-time FET-sensor response for TMB oxidation by HRP at different reagent concentrations under reaction initiation by addition of H<sub>2</sub>O<sub>2</sub>. (A) Various H<sub>2</sub>O<sub>2</sub> concentrations at 7.4 nM HRP, 500 μM TMB, reaction initiation at 60 s. (B) Various TMB concentrations at 18 nM HRP, 200 μM H<sub>2</sub>O<sub>2</sub>, reaction initiation at 35 s; arrow shows the area of HRP-I formation reaction. (C) Various TMB concentrations at 5 nM HRP, 200 μM H<sub>2</sub>O<sub>2</sub>, reaction initiation at 113 s. (D) Various HRP concentrations at 500 μM TMB, 200 μM H<sub>2</sub>O<sub>2</sub>, reaction initiation at 50 s; arrow shows the area of HRP-I formation reaction.

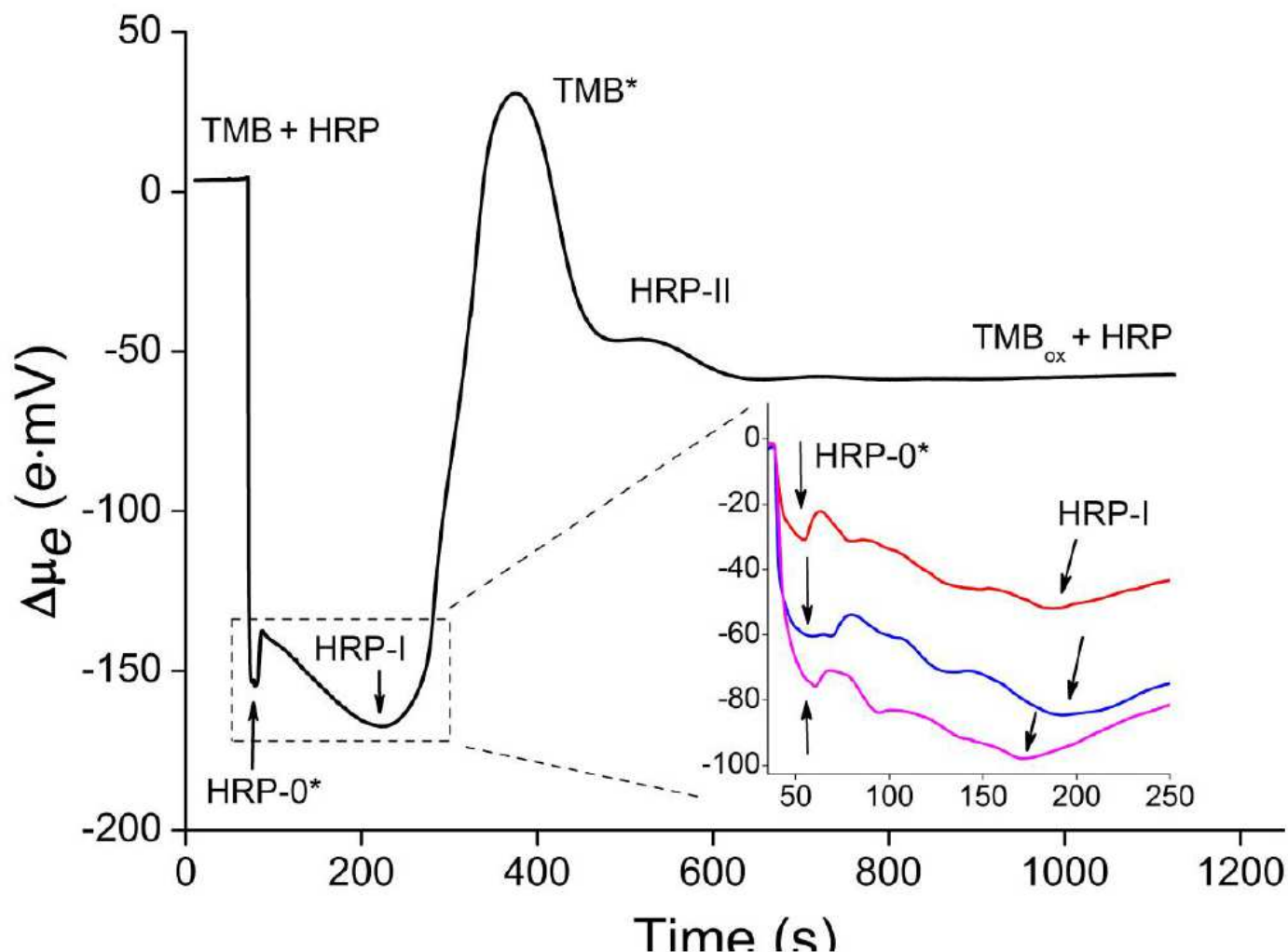


**Figure 5**

Energy pathway equal to the relative changes in Gibbs free energy during the reaction of TMB oxidation catalyzed by HRP with suggested intermediates (50 μM HRP, 500 μM TMB, 200 μM H<sub>2</sub>O<sub>2</sub>). Reaction was initiated by addition of H<sub>2</sub>O<sub>2</sub> at 70 s. Enlarged area: 0.05 μM HRP, 200 μM H<sub>2</sub>O<sub>2</sub>; red, 70 μM TMB; blue, 90 μM TMB; purple, 200 μM TMB.

## Supplementary Files

This is a list of supplementary files associated with this preprint. Click to download.

- [280350supp249489qk8wnf.pdf](#)